

Fluctuation of the background sky in the Hubble Extremely Deep Field (XDF) and its origin

Toshio MATSUMOTO^{1,*} and Kohji TSUMURA^{2,3}

¹Department of Space Astronomy and Astrophysics, Institute of Space and Astronautical Science, Japan Aerospace Exploration Agency, 3-1-1 Yoshinodai, Chuo-ku, Sagami-hara, Kanagawa 252-5210, Japan

²Department of Natural Science, Faculty of Knowledge Engineering, Tokyo City University, 1-28-1 Tamazutsumi, Setagaya, Tokyo 158-8557, Japan

³Frontier Research Institute for Interdisciplinary Science, Tohoku University, 6-3 Aoba, Aramaki, Aoba-ku, Sendai, Miyagi 980-8578, Japan

*E-mail: matsumo@ir.isas.jaxa.jp

Received 2019 February 17; Accepted 2019 May 30

Abstract

We performed a fluctuation analysis of the Hubble Extremely Deep Field (XDF) at four optical wavelength bands and found large fluctuations that are significantly brighter than those expected for ordinary galaxies. Good cross-correlations with flat spectra are found down to $0''.2$, indicating the existence of a spatial structure even at the $0''.2$ scale. The detected auto- and cross-correlations provide a lower limit of $24 \text{ nW m}^{-2} \text{ sr}^{-1}$ for the absolute sky brightness at 700–900 nm, which is consistent with previous observations. We searched for candidate objects to explain the detected large fluctuation using the catalog of the Hubble Ultra Deep Field (UDF), and found that the surface number density of faint compact objects (FCOs) rapidly increases toward the faint end. Radial profiles of FCOs are indistinguishable from the point spread function (PSF), and the effective radius based on de Vaucouleur's law is estimated to be smaller than $0''.02$. The spectral energy densities (SEDs) of FCOs follow a power law at optical wavelengths, but show greater emission and structure at $\lambda > 1 \mu\text{m}$. Assuming that the FCOs are the cause of the excess brightness and fluctuations, the faint magnitude limit is 34.9 mag for the *F775W* band, and the surface number density reaches $2.6 \times 10^3 \text{ arcsec}^{-2}$. Recent γ -ray observations require that the redshift of FCOs must be less than 0.1, if FCOs are the origin of the excess optical and infrared background. Assuming that FCOs consist of missing baryons, the mass and luminosity of a single FCO range from 10^2 to 10^3 solar units, and the mass-to-luminosity ratio is significantly lower than 1.0 solar unit. The maximum effective radius of an FCO is 4.7 pc. These results and the good correlation between the near-infrared and X-ray background indicate that FCOs could be powered by the gravitational energy associated with black holes.

Key words: cosmology: observations — galaxies: evolution — infrared: diffuse background

1 Introduction

The extragalactic background light (EBL) is thought to represent the energy density of the universe, and has been

observed over a wide range of wavelengths. In the optical and near-infrared regions, EBL observations have been performed and excess brightness over the integrated light of

known celestial sources has been detected based on the data of Hubble Space Telescope (HST) (Bernstein 2007; Kawara et al. 2017), Diffuse InfraRed Background Experiment/COsmic Background Explorer (COBE) (Hauser et al. 1998; Wright 1998; Wright & Reese 2000; Gorjian et al. 2000; Cambr sy et al. 2001; Levnson et al. 2007; Sano et al. 2015, 2016), Near InfraRed Spectrometer (NIRS)/InfraRed Telescope in Spce (IRTS) (Matsumoto et al. 2005, 2015), AKARI (Tsumura et al. 2013), and Cosmic Infrared Background ExpeRiment (CIBER) (Matsuura et al. 2017) etc. The detection of EBL is not simple due to the bright foreground emission known as the zodiacal light. However, the zodiacal light is so sufficiently smooth (Pyo et al. 2012) for the detection of the EBL fluctuation that the measurements have been conducted with Spitzer (Kashlinsky et al. 2005, 2007, 2012), AKARI (Matsumoto et al. 2011; Seo et al. 2015), HST (Thompson et al. 2007; Mitchell-Wynne et al. 2015; Donnerstein 2015), CIBER (Zemcov et al. 2014), and IRTS (Kim et al. 2019). Researchers have found excess fluctuation that cannot be explained by ordinary galaxies (Helgason et al. 2012).

The origin of the excess brightness and fluctuation has been examined by numerous researchers. First stars are an attractive candidate, however, recent evolution models based on the observations of high-redshift galaxies indicate that the brightness and fluctuation caused by first stars are much lower than the observed excesses (Cooray et al. 2012b; Yue et al. 2013a). As an origin of the excess fluctuation, Cooray et al. (2012a) proposed the intra-halo light (IHL) defined as the emission from stars expelled into the intergalactic space due to collisions and/or merging of galaxies at low redshifts. IHL is advantageous in energetics problems, however, no observational evidence of IHL has yet been reported. Furthermore, there are difficulties in invoking IHL to explain large fluctuations at the degree scale (Kim et al. 2019) and the excess EBL. Yue et al. (2013b) explained the fluctuation observed with Spitzer using direct collapsed black holes (DCBHs) at high redshifts. DCBHs are favorable for explaining the cross-correlation between the near-infrared and X-ray background (Cappelluti et al. 2013, 2017; Mitchell-Wynne et al. 2015), however, difficulties remain for explaining the observed fluctuation at $\lambda < 1 \mu\text{m}$ (Mitchell-Wynne et al. 2015; Zemcov et al. 2014).

At present, there is no known source that can explain all of the EBL observations. To obtain new observational evidence, we performed a fluctuation analysis for the deepest images, the Hubble Extreme Deep Field (XDF) (Illingworth et al. 2013) with four filter bands (*F435W*, *F606W*, *F775W*, and *F850LP*). Our approach is very similar to the fluctuation analysis of the NICMOS Ultra Deep Field (NUDF) by Thompson et al. (2007) and

Donnerstein (2015) at 1.0 and 1.6 μm , and of the Cosmic Assembly Near-Infrared Deep Extragalactic Legacy Survey (CANDELS) field at optical and near-infrared wavelengths (Mitchell-Wynne et al. 2015). The detection limits of the XDF sources are ~ 30 mag in AB magnitude system (Illingworth et al. 2013), which are two or three magnitudes deeper than those in previous analyses. This value implies that the contribution of the ordinary faint galaxies to the surface brightness in the XDF blank sky is very low, which may enable one to observe the nature of unknown objects. Cross-correlations between wavelength bands are also analyzed to determine the spatial structure of the fluctuation.

We have attempted to identify candidates of the unknown sources in the XDF, and discovered the faint compact objects (FCOs). Assuming that FCOs are responsible for the excess brightness and fluctuation in the sky, we examined the properties of FCOs based on the Ultra Deep Field (UDF) (Beckwith et al. 2006) and ultraviolet UDF (UVUDF) (Rafelski et al. 2015) catalogs.

This paper is organized as follows. In section 2, we present a fluctuation analysis of the XDF data, and the absolute sky brightness estimated from the detected fluctuation. In section 3, we examine the properties of FCOs as the origin of the detected EBL excess. In section 4, we discuss the possible origin of FCOs, and a summary is given in section 5.

2 Fluctuation analysis

XDF images are the deepest images observed with ACS/WFC aboard the HST (Illingworth et al. 2013). The field of the optical bands is 11 arcmin² with images obtained from five filter bands. Their filter names and central bandwidths are *F435W* (432.3 nm), *F606W* (591.2 nm), *F775W* (769.9 nm), *F814W* (818.6 nm), and *F850LP* (906.0 nm). We did not analyze the *F814W* image, because the integration time for this filter is significantly lower than that of other bands, and additionally no catalog is available for this band. We used XDF images from a publicly available site,¹ where images of two pixel resolution levels (30 and 60 mas) are available. We used images with a resolution of 60 mas for the fluctuation analysis because these images have better sensitivity for diffuse extended sources.

The integration times of the XDF images are not uniform; instead, the times vary for different locations. To achieve an accurate analysis, we extracted the central region where the integration times are the longest and highly uniform (see figure 3 in Illingworth et al. 2013). The left-hand panel of figure 1 shows an extracted image for *F775W*.

¹ (<https://archive.stsci.edu/prepds/xdff/>).

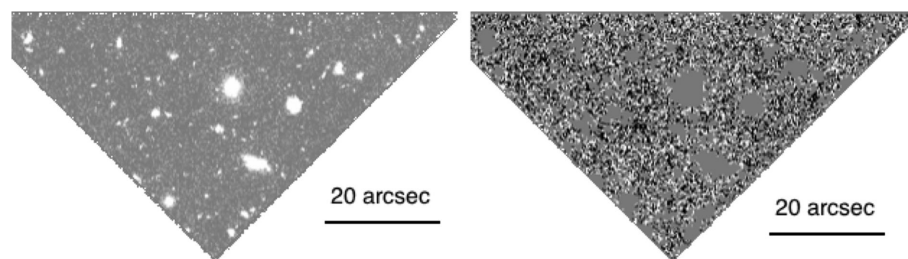


Fig. 1. Extracted image for *F775W*. The left- and right-hand panels show images before and after masking, respectively. We changed the contrasts of the two images to display the structure clearly.

A mask of the XDF images for fluctuation analysis was created by combining images for the four optical bands (*F435W*, *F606W*, *F775W*, and *F850LP*). The mask was created in four steps. First, we masked all pixels that are brighter than 2σ , where σ is the dispersion of the brightness distribution of the image. Almost all sources are masked in this procedure, but pixels surrounding bright objects are not perfectly masked because the diffuse extended wing around a bright object remains. Thus, we treated the adjacent 3×3 pixels of each pixel (including the original pixel) for masking to discriminate extended features. In the second step, we additionally masked all nine pixels when more than four pixels are brighter than 1σ . In the third step, we again masked all nine pixels when more than six pixels are already masked. As the fourth step, we repeated the third process to expand the mask by one more layer. Finally, 53.3% of the pixels remained after this masking procedure, and the extended wings of the objects were well masked (figure 18). The obtained mask was applied to the four XDF optical images. The right-hand panel of figure 1 shows a masked image for the *F775W* band. The brightness distributions of the masked images are very close to a Gaussian distribution (figure 19). We defined the limiting magnitudes as 3σ in the statistics for the average of a 2×2 pixel square, which corresponds to 33.17, 33.62, 33.36, and 32.80 in AB magnitude for *F435W*, *F606W*, *F775W*, and *F850LP*, respectively. Supplementary information on the masking is given in appendix 1.

For the masked images, we performed a two-dimensional Fourier transformation and obtained power spectra, $P_2(q)$, and fluctuations, $[q^2 P_2/(2\pi)]^{1/2}$, as a function of wavenumber, q , following previously reported analysis (Thompson et al. 2007).

Since the fluctuation is artificially reduced at large angles when the number of the masked pixels is large, we applied a simple correction for the masking effect. We created 100 simulation images with the same fluctuation spectrum as the XDF *F606W* image, and estimated a recovery factor, defined as the ratio of the fluctuation levels before and

after masking at a specific wave number, q . The recovery factor shows a strong dependence on the angular scale and amounts to ~ 1.5 at the largest angle (figure 19). We applied the recovery factors to the fluctuation spectra, but the correction did not substantially influence the forthcoming analysis.

Figure 2 shows the obtained auto-fluctuations. Considering that the point spread function (PSF) is $\sim 0''.1$, we plot the data for angles larger than $0''.2$. Shot noise at small angles and flat spectra at $10''$ – $30''$ are commonly present in these plots.

In figure 2, we compare the observed fluctuations with those expected for ordinary galaxies, adopting the surface number density and magnitude relations described in the next section (figure 7). The black dotted lines indicate fluctuations obtained via simulation analysis assuming a random distribution of ordinary galaxies that are fainter than the limiting magnitudes of 30, 32, and 34 mag. The solid black lines correspond to the limiting magnitudes of the XDF masked images.

We estimated the contribution of the clustering of faint galaxies based on the model by Helgason, Ricotti, and Kashlinsky (2012), who examined the fluctuation due to one-halo and two-halo terms. The fluctuation of one-halo term shows a similar feature (shot noise) to that of the random distribution, but is a few times lower than that of the random distribution. The profile of two-halo term has a peak at $\sim 1500''$ and does not depend on the wavelengths. Furthermore, the absolute value at the peak is proportional to the integrated light of galaxies (ILG) fainter than the limiting magnitude. The ILG in our analysis ($\sim 0.06 \text{ nW m}^{-2} \text{ sr}^{-1}$) provides the peak fluctuations of two-halo term to be $\sim 2 \times 10^{-3} \text{ nW m}^{-2} \text{ sr}^{-1}$, which is negligible compared to the detected fluctuations.

Figure 2 and the above considerations clearly show that the detected fluctuations are significantly larger than those expected for ordinary galaxies, indicating the presence of unknown celestial objects.

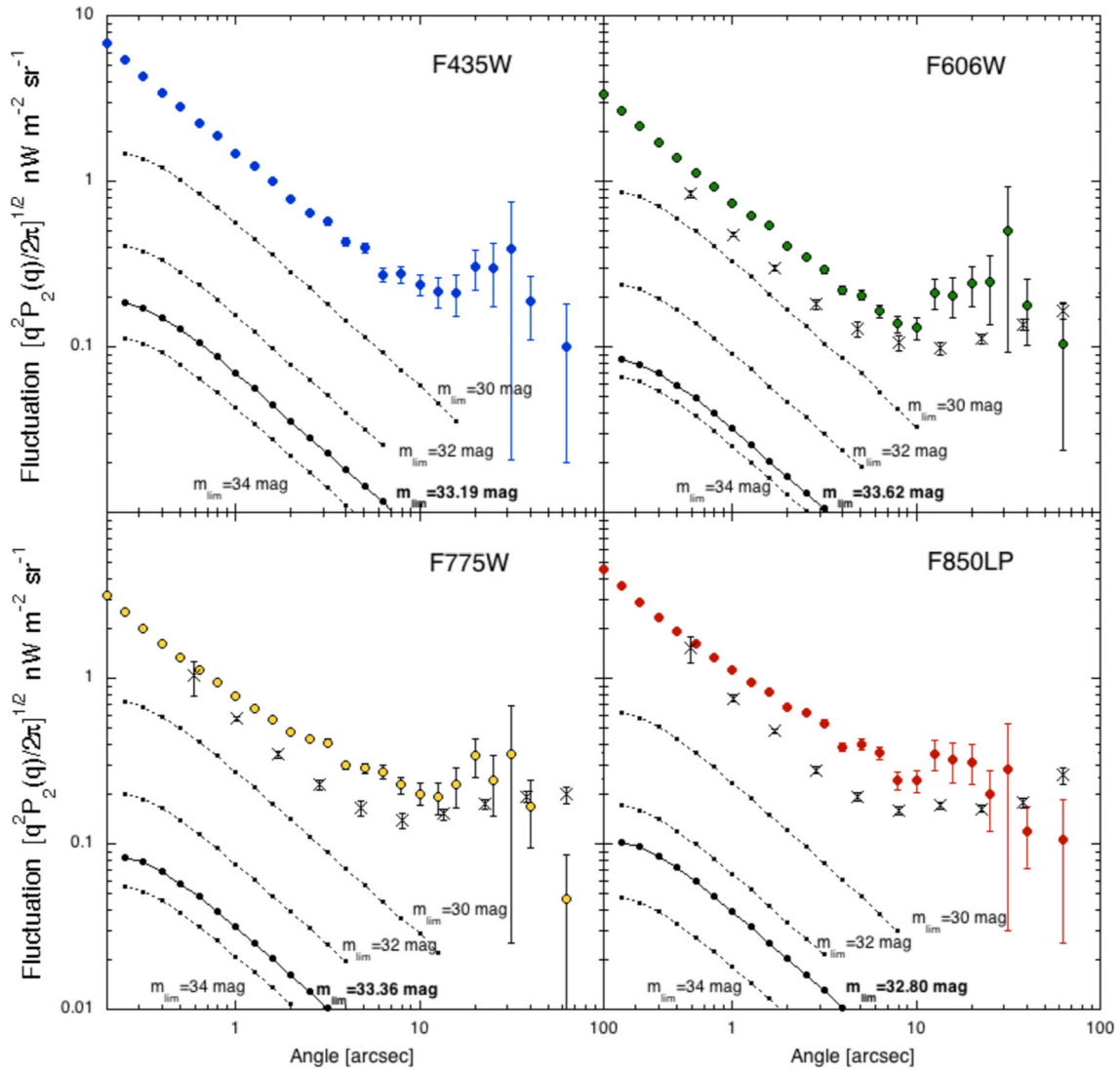


Fig. 2. Auto-correlations of the masked XDF images for four optical bands. The crosses denote data obtained for the CANDELS field (Mitchell-Wynne et al. 2015). The dotted lines represent simulated fluctuations for ordinary galaxies with three different limiting magnitudes, m_{lim} . The solid lines indicate the same result obtained for limiting magnitudes in our XDF fluctuation analysis. (Color online)

In figure 2, fluctuations analyzed for imaging data from the CANDELS field are plotted as crosses (Mitchell-Wynne et al. 2015). Fluctuations for the *F435W* were not analyzed for the CANDELS field. The fluctuation spectra for the CANDELS field are basically consistent with our XDF fluctuations, but the absolute values are slightly lower than those of the XDF images. This difference is most likely caused by variations in image quality. The observation area of the CANDELS field is much wider than that of the XDF, whereas the limiting magnitudes of the CANDELS survey are a few magnitudes lower than that of the XDF, although the limiting magnitudes are not explicitly reported by Mitchell-Wynne et al. (2015). Furthermore,

the number of overlapping images in the CANDELS analysis is not uniform; in the most extreme case, there is a ten-fold difference. These differences make it difficult to qualitatively compare the shot noise of the CANDELS field with the present result.

The contribution of the foreground signal is negligible. The fluctuation of the zodiacal light is less than 0.03% (Pyo et al. 2012) corresponding to $\sim 0.1 \text{ nW m}^{-2} \text{ sr}^{-1}$. Furthermore, the overlapping of a large number of images observed during different seasons substantially reduces the fluctuation, since fluctuation of the zodiacal light is not fixed on the sky. Another foreground emission, diffuse Galactic light (DGL), shows a fluctuation proportional to

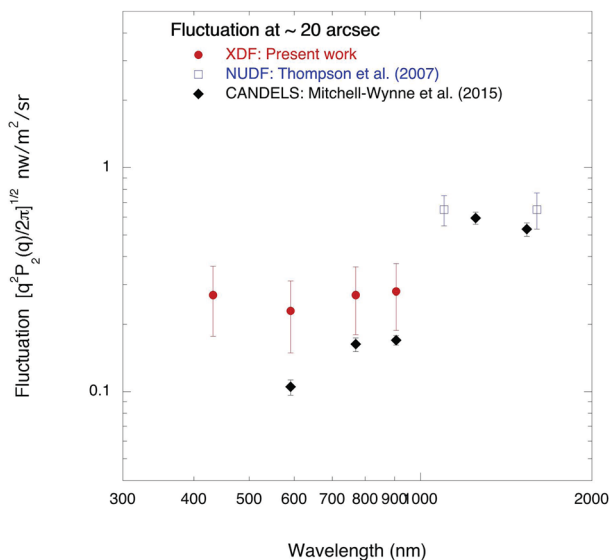


Fig. 3. Dependence of the average fluctuations at $\sim 20''$ on the wavelength (red filled circles). Fluctuations for the NUDF (Thompson et al. 2007) and CANDELS (Mitchell-Wynne et al. 2015) fields are also plotted as open squares and solid diamonds, respectively. (Color online)

the angular scale (Mitchell-Wynne et al. 2015), thus, DGL fluctuation is negligible at the small angular scales utilized in this study.

We attempted to perform a fluctuation analysis of the infrared XDF images; however, the absolute values of their fluctuations are much lower than those of NUDF, as reported by Thompson et al. (2007) and CANDELS, as reported by Mitchell-Wynne et al. (2015). This difference is most likely due to the strong spatial filters applied to correct for the effect of earthshine in the infrared XDF images (Illingworth et al. 2013). Therefore, we do not include a fluctuation analysis of the infrared images in this paper.

Figure 3 shows the average fluctuations measured in the flat region ($\sim 20''$) as well as those of NUDF (Thompson et al. 2007) and CANDELS (Mitchell-Wynne et al. 2015) at infrared wavelengths. Figure 3 shows that the fluctuations in the infrared bands are larger than those in the optical bands.

Figure 4 displays the cross-correlations between wavelength bands. Shot noise appears for the cross-correlations with *F435W* but is not observed for the cross-correlations with the three other bands, indicating that the auto-correlation shot noises at small angular scales can be ascribed to photon noise and/or readout noise. The remaining shot noise for the cross-correlations with the *F435W* band may be due to faint ordinary galaxies, which will be examined in the next section.

In figure 4, cross-correlations for the CANDELS field are plotted (Mitchell-Wynne et al. 2015). The basic features are similar to those of the XDF, however, shot noise components remain even for the three longer wavelength bands. This result can be ascribed to shot noises arising from the ordinary galaxies since the limiting magnitudes in the CANDELS study are much lower than those in the present work.

The correlations among the three longer wavelength bands are excellent. In particular, *F775W* \times *F850LP* shows an almost perfect correlation at angles larger than $10''$. The correlation spectra are marginally flat and extend down to $0''.2$, indicating the existence of the sky structure even at the $0''.2$ scale. In other words, the sky is filled with unknown objects, even at the $0''.2$ scale. The surface number density for one object in 0.2 square arcseconds corresponds to $3.2 \times 10^8 \text{ degree}^{-2}$. This value is a lower limit and is much larger than that of ordinary galaxies, as is shown in the next section.

Large correlations imply that the considerable sky brightness is due to unknown objects. The auto-fluctuation spectra of the *F775W* and *F850LP* bands must be larger than the cross-correlation spectrum, *F775W* \times *F850LP*, since there may be an additional uncorrelated fluctuation component in each band. Therefore, we assume that the cross-correlation spectrum is the minimum of the auto-fluctuation spectra for both the *F775W* and *F850LP* bands. We created simulated images with a fluctuation spectrum equal to the cross-correlation spectrum (*F775W* \times *F850LP*) and obtained a dispersion of 1σ for the brightness distribution. Using 10 trials, we obtained a 1σ value of $8.10 \pm 0.01 \text{ nW m}^{-2} \text{ sr}^{-1}$. Since the sky brightness must always be positive, we take the 3σ brightness, $24 \text{ nW m}^{-2} \text{ sr}^{-1}$, as the lower limit of the absolute sky brightness in the *F775W* and *F850LP* bands. Moreover, we estimated the ILG to be fainter than the limiting magnitude based on the surface number density magnitude relation (solid black lines in figure 7) and obtained 0.053 and $0.056 \text{ nW m}^{-2} \text{ sr}^{-1}$ for *F775W* and *F850LP* bands, respectively, which are negligible compared with the obtained lower limit. Furthermore, the detected lower limit is too bright to be explained by the IHL (Cooray et al. 2012a).

Figure 5 presents a summary of the observed excess brightness over the ILG. The obtained lower limit is indicated by a thick horizontal red bar, the width of which covers the wavelength range of *F775W* and *F850LP*. The solid black line indicates the model ILG based on the deep survey and model galaxy (Totani & Yoshii 2000; Matsumoto et al. 2005). The results of other authors represent the excess brightness after subtracting the model ILG

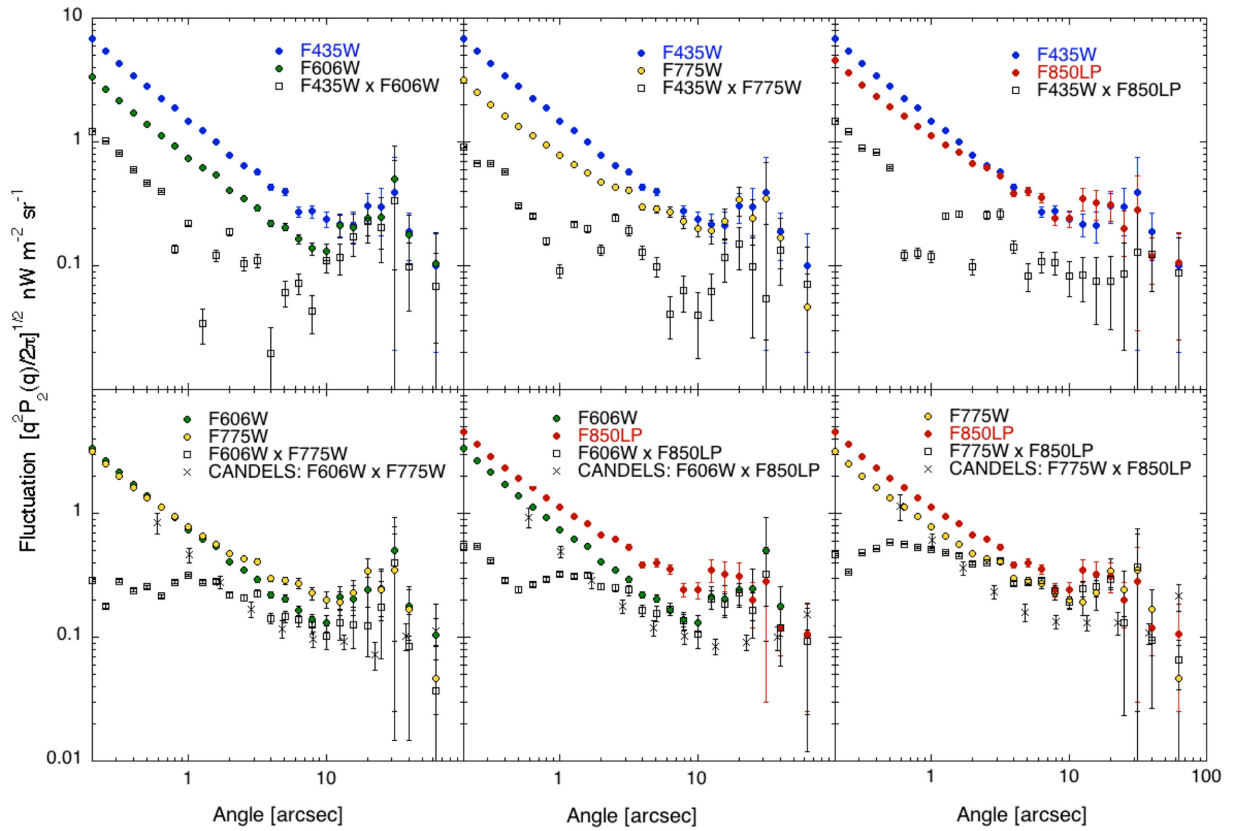


Fig. 4. Cross-correlations for the XDF field. The squares represent the cross-correlation for the two wavelength bands whose auto-correlations are given in figure 3 in each panel. The crosses represent cross-correlations for the CANDELS field (Mitchell-Wynne et al. 2015). (Color online)

from the observed EBL, depending on the limiting magnitudes. Figure 5 indicates that our findings are consistent with results acquired for CIBER/LRS (Matsuura et al. 2017) and HST (Bernstein 2007). Zemcov et al. (2017) analyzed data from the Long Range Reconnaissance Imager instrument on NASA's New Horizons mission for the wavelength range of 440–870 nm and reported an upper limit, $19.3 \text{ nW m}^{-2} \text{ sr}^{-1}$, beyond the Jovian orbit, which is lower than our lower limit. However, their result does not contradict our findings, since there exists a large systematic error, $+10.3 \text{ nW m}^{-2} \text{ sr}^{-1}$, in their result. Mattila et al. (2017) performed a spectroscopy study of the stellar Fraunhofer lines toward a dark cloud at high galactic latitudes, and estimated the EBL by comparing the line strength measured inside and outside the dark cloud. The authors reported the EBL detection at 400 nm with an upper limit at 520 nm (green symbols in figure 5), and reported that the detected EBL was too high to be explained by the ILG. The excess brightness detected in that study is slightly lower than the value in this work, however, two results are not inconsistent, considering the large errors and the difference in wavelengths. Kawara et al. (2017) reported the detection of isotropic emission at $0.2\text{--}0.6 \mu\text{m}$ using the HST/FOS

sky spectra, which is consistent with the EBL detected by Bernstein (2007). The authors attributed the isotropic emission to the solar system origin, because the spectrum is similar to that of the zodiacal light. However, it is possible that part of the detected isotropic emission is EBL. Matsuoka et al. (2011) analyzed the data from Imaging Photopolarimeter onboard Pioneer 10 and obtained the optical EBL beyond the Jovian orbit, which is consistent with the ILG. However, we do not include their data in figure 5 because they did not account for the effect of instrumental offset (Matsumoto et al. 2018).

Thus, in summary, our analysis reveals that there exists bright excess background light, even at optical wavelengths, and that the energy density in the optical and near-infrared wavelengths is a few times or more higher than that previously thought (black line).

3 Fluctuation source

3.1 Faint compact objects (FCOs)

Fluctuation analysis reveals the presence of unknown celestial objects that are densely distributed throughout the sky.

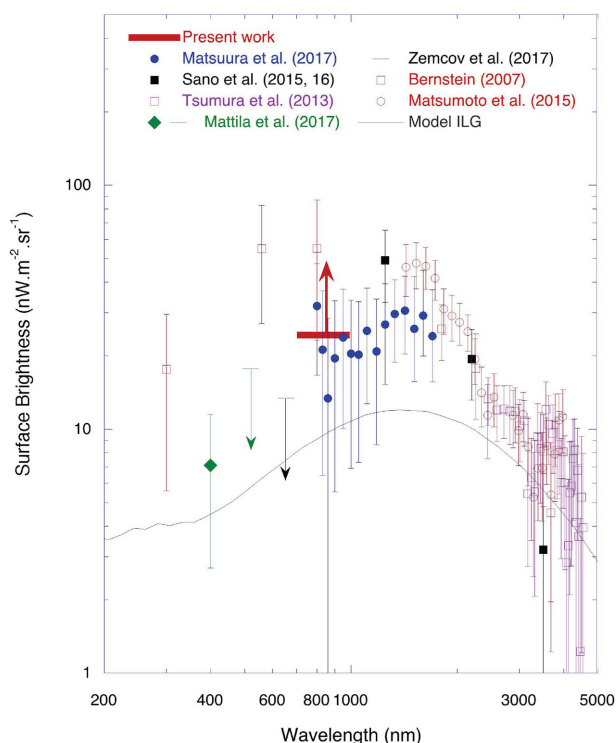


Fig. 5. Summary of observations of the optical and near-infrared excess background over the integrated light of galaxies (ILG). The thick horizontal red bar indicates the lower limit we obtained. The solid black line represents the model ILG which includes all galaxies (Totani & Yoshii 2000; Matsumoto et al. 2005). (Color online)

To identify these unknown objects, we carefully examined XDF images and found that the density of compact objects dramatically increases toward the faint end. We examined the nature of these objects based on the catalog of UDF objects reported by Beckwith et al. (2006), since an XDF catalog is not available.

In figure 6, we present UDF objects in a magnitude/stellarity diagram, where objects that were identified as stars in Pirzkal et al. (2005) are removed. In figure 6, 8918 objects are plotted for the *F775W* band for which stellarities are measured in the UDF catalog. The stellarity index in SExtractor was developed to identify stars in images (Bertin & Arnouts 1996) by evaluating the compactness and the presence of an extended envelope. Objects with a stellarity value larger than 0.8 are usually regarded as stars. Figure 6 shows a group of high-stellarity objects in the faint region which we denote as FCOs. In figure 6, the fainter-magnitude FCOs have lower stellarities; however, this trend is most likely not an intrinsic feature. Confusion with the sky fluctuations extending down to the 0".2 scale is more problematic for faint objects, which reduces their apparent stellarity.

A somewhat arbitrary line is drawn in figure 6 to separate FCOs from ordinary galaxies. The number of FCOs,

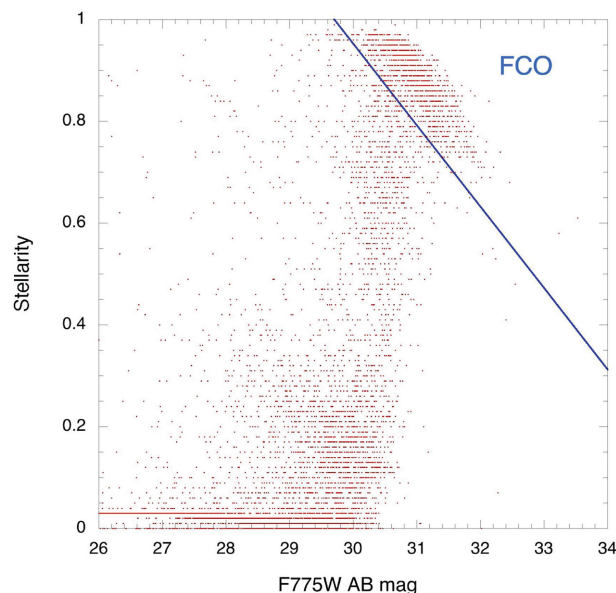


Fig. 6. Stellarity/magnitude (*F775W*) diagram of 8918 objects. Data points for objects with the same values are overlaid. The blue solid line is drawn rather arbitrarily to separate FCOs from ordinary galaxies. (Color online)

defined as objects located to the upper right of the solid line, is 1283. The catalog of the detected FCOs is given in the Supplementary Data section, available online. For a detailed analysis, we retrieved 649 FCOs whose stellarities are larger than 0.9.

Figure 7 shows the cumulative number counts as a function of the apparent magnitude, m . The filled squares and filled circles represent all objects and objects with stellarity > 0.9 , respectively. Figure 7 clearly shows that the surface number density of FCOs increases much more dramatically than that of all objects toward the faint end. We fit the slopes for FCOs in the *F775W* band using a power law (red lines) such that the residual numbers of objects in the bright region are constant (open squares). The result, $\propto 10^{1.2m}$, is much steeper than the isotropic distribution, $\propto 10^{0.4m}$, and corresponds to the density distribution, $n(r) \propto r^3$, where $n(r)$ is the spatial number density and r is the radial distance. The surface number density of FCOs must peak at a certain magnitude; otherwise the sky brightness would diverge.

The *F606W* and *F850LP* bands show a sharp increase, similar to that of the *F775W* band, but the slopes are lower than that of *F775W*, most likely because of color scattering. For the *F435W* band, it is difficult to separate the FCOs because ordinary galaxies with large stellarities are not negligible, even at 30 mag. This trend may account for why shot noise remains for the cross-correlation with the *F435W* band in figure 4. We extrapolated the slopes of all objects toward the faint region to be $\sim 10^{0.244m}$

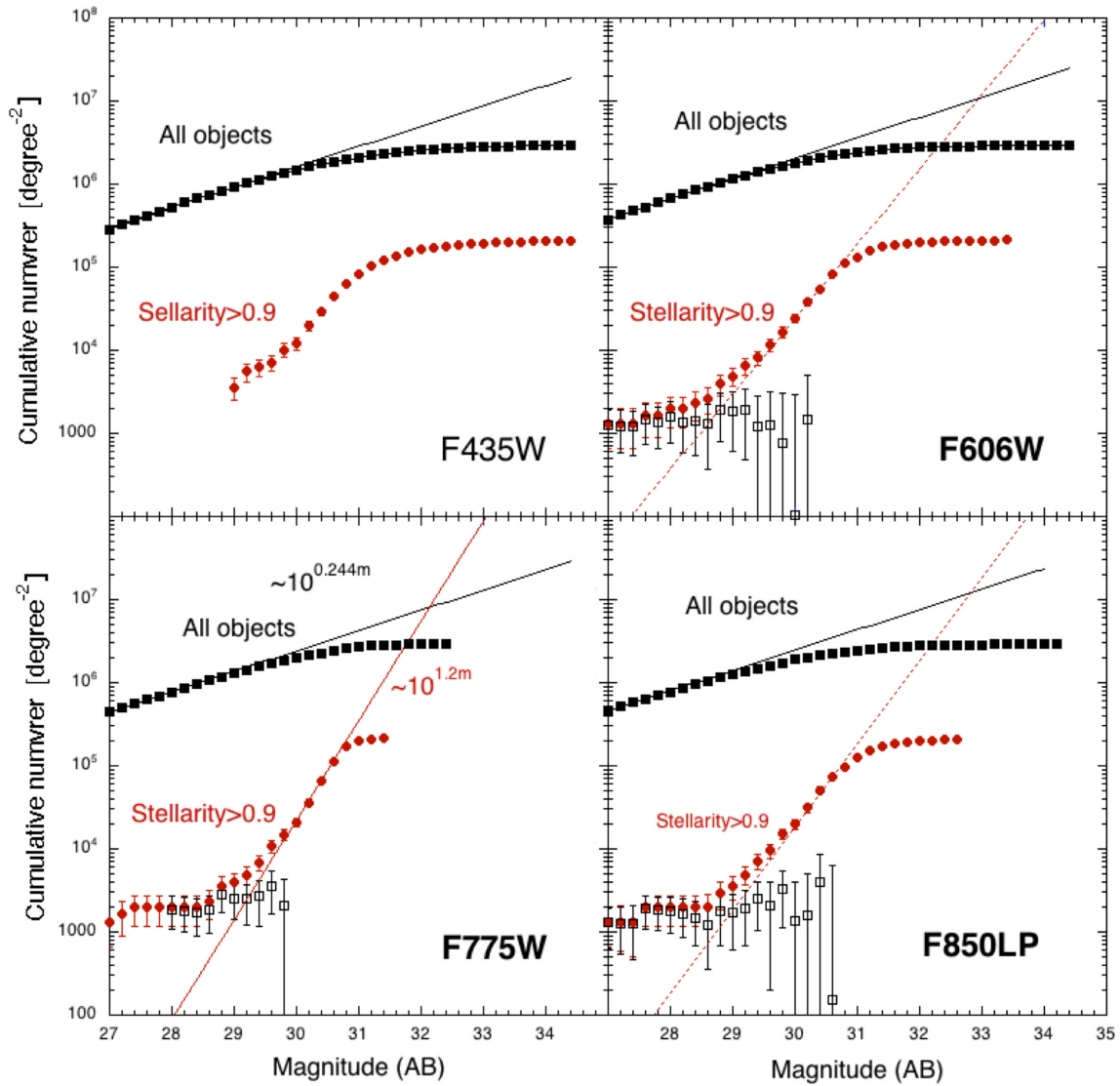


Fig. 7. Cumulative surface number densities of four optical bands as a function of the apparent magnitude, m . The filled squares and filled circles represent all objects and objects with stellarity > 0.9 , respectively. The open squares denote the surface number density of ordinary galaxies with stellarity > 0.9 . (Color online)

by applying the evolution model (Helgason et al. 2012), which was used to estimate the fluctuation of ordinary galaxies in figure 2. Because the model predicts smooth slopes up to 32 mag, the turn over of all the detected objects are due to the detection limit. The turn overs of the FCOs occur at slightly fainter magnitudes than those for all objects because the detection limit of a compact object is better than that of an extended object. If we assume a simple extrapolation for FCOs and consider the total number of FCOs to be twice the value given in figure 7, the surface number densities of FCOs exceed those of ordinary galaxies at 31.8 mag for the *F775W* band. If we assume that the excess surface brightness is due to the integrated light of FCOs, the lower limit of

the surface brightness of $24 \text{ nW m}^{-2} \text{ sr}^{-1}$ implies a cut-off magnitude of 34.9 for the *F775W* band. In this case, the cumulative surface number density is determined as $3.35 \times 10^{10} \text{ degree}^{-2}$, $2.6 \times 10^3 \text{ arcsec}^{-2}$, or 1.38×10^{15} for the entire sky.

To evaluate the validity of using stellarity index, we examined the compactness of FCOs using images with a pixel resolution of 30 mas. We divided the images into annular rings with a width of $0''.03$ and obtained the average surface brightness in units of $\lambda I_\lambda: \text{nW m}^{-2} \text{ sr}^{-1}$ for each ring. Using the same procedure, we obtained radial profiles of the PSF using stellar images for comparison with those for the FCOs. Figure 8 shows a typical example of the radial profiles and XDF images for a bright FCO, UDF8942, which

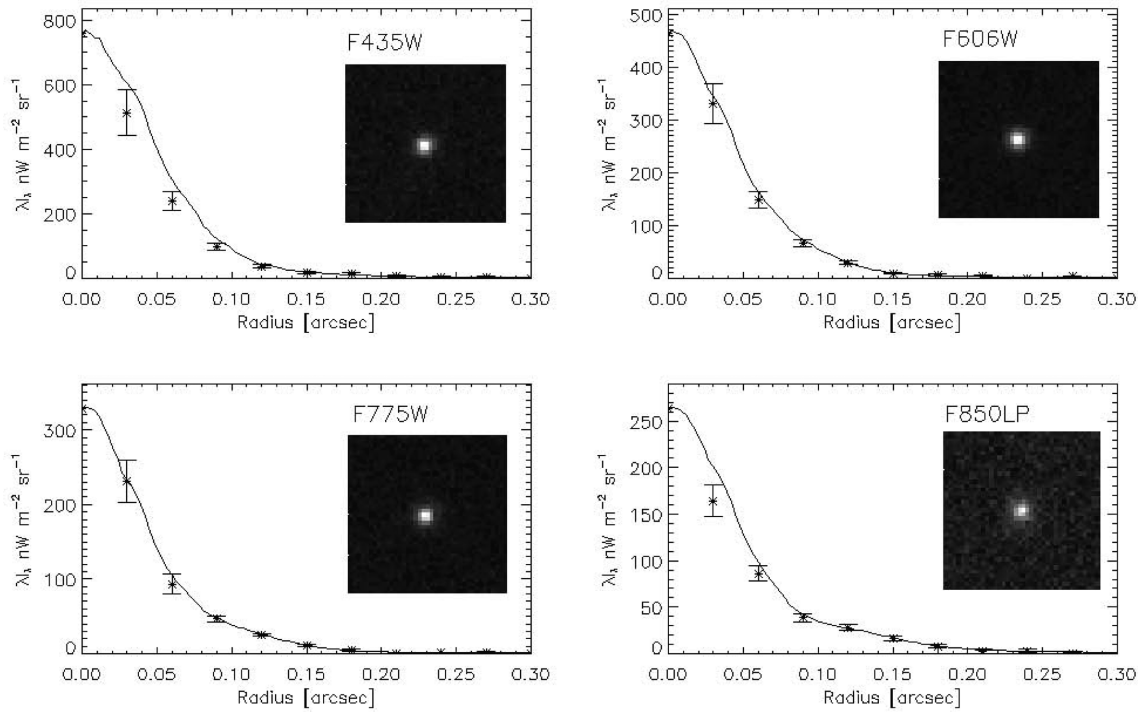


Fig. 8. Radial profiles and XDF images of a bright FCO, UDF8942, for four optical bands. The solid lines represent the PSF obtained from stellar images. Image scales are 41×41 pixel², or 1.23×1.23 arcsec².

are not distinguishable from stellar images for all wavelength bands.

Furthermore, we selected 48 bright FCOs as an order of the average errors for the four wavelength bands and examined their radial profiles in the combined *F606W* and *F775W* images, since the signal-to-noise ratios for the *F435W* and *F850LP* bands are relatively poor. The obtained radial profiles for the 48 bright FCOs are shown in figure 20 in appendix 2. These profiles are highly similar to the PSF, indicating that the stellarity in the UDF catalog is a reliable index for identifying the compact sources. The two bright objects, #1 (UDF9397) and #3 (UDF6732), are identified as quasars (table 1) which have radial profiles that are fairly consistent with the PSF, which confirms the validity of our analysis. Objects #2 (UDF7025), #4 (UDF4070), #5 (UDF8230), #6 (UDF5711), #8 (UDF2087), and #12 (UDF5550) show a slight enhancement at $0''.1$ – $0''.2$, which suggests that they may be ordinary galaxies with an extended halo or disk. Object #36 (UDF1240) shows a deviation of the radial profile from the PSF, which could be ascribed to source confusion, as there exists another source in the immediate vicinity. For the other FCOs, the radial profiles (figures 8 and 20) are not distinguishable from the PSF within the errors, and extended envelopes are not detected.

The detection limits of the envelope surface brightness are determined for the structure of the sky, with a 3σ fluctuation level for 0.12×0.12 arcsec² that amounts to $\lambda I_{\lambda} \sim 5.3, 2.58, 2.52$, and 3.58 nW m^{−2} sr^{−1} for the *F435W*, *F606W*, *F775W*, and *F850LP* bands, respectively, which correspond to 28.3, 28.7, 28.5, and 27.9 mag arcsec^{−2}. The exponential disk of spiral galaxies has a much brighter surface brightness (< 26 mag arcsec^{−2}) for scales larger than 1 kpc. Since the minimum angular scale of 1 kpc corresponds to $0''.12$ at $z \sim 1.6$, the radial profiles of FCOs indicate that extended disks do not exist in the FCOs except for the six bright cases. However, we must also consider that the surface brightness rapidly decreases at high redshifts.

To estimate the compactness of FCOs qualitatively, we calculated convolved radial profiles with the PSF for dwarf spheroidals, which follow de Vaucouleur's law,

$$I(r) = I_e \exp\{-7.67[(r/r_e)^{1/4} - 1]\}, \quad (1)$$

where r_e is the effective radius in which half of the total light is contained. Figure 9 shows a comparison of the PSF for the *F775W* band and the convolved images for $r_e = 0''.02, 0''.05, 0''.1$, and $0''.2$. Figure 9 indicates that a larger r_e corresponds to a more extended envelope, while the r_e of the FCOs is at most $0''.02$. Since the angular distance has

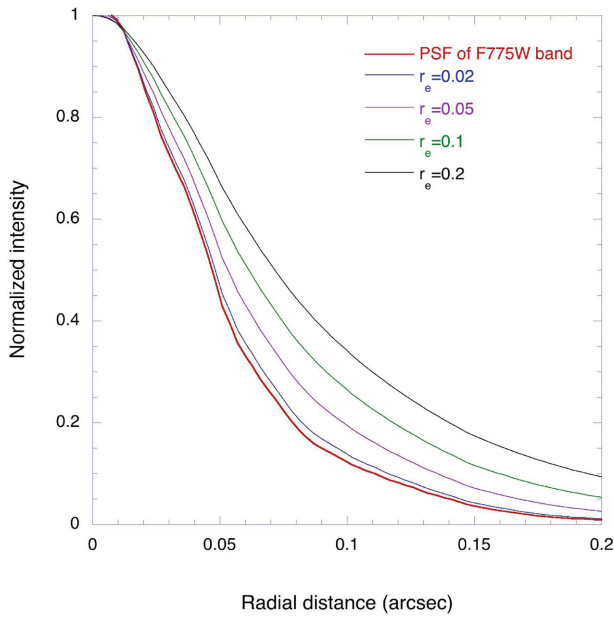


Fig. 9. PSF (red lines) for the *F775W* band compared with convolved images of the radial distribution of dwarf spheroidals that follow de Vaucouleur's law for different effective radii, r_e . (Color online)

a maximum at $z \sim 1.6$, where $0''.1$ corresponds to 860 pc, the physical size of r_e must be smaller than 172 pc. This size corresponds to the low end of the size range of ordinary dwarf spheroidals (Zhang & Bell 2017).

As a next step, we examined the photometric data. Figure 10 presents a color–color diagram of 128 FCOs that have average errors of less than 0.2 mag. The left- and right-hand panels show $(F606W - F775W)/(F435W - F606W)$ and $(F775W - F850LP)/(F606W - F775W)$, respectively. The straight lines indicate the loci of a blackbody with

a temperature range from 4000 K to 14000 K. Although a clear sequence is not found due to the large errors, figure 10 indicates that the color temperatures are fairly high (~ 10000 K), and the centroids are close to the point of origin. This result implies that the magnitudes of the four optical bands are similar, that is, the spectral energy density (SED) in units of λI_λ shows a dependence on λ^{-1} .

The SED is a key factor in understanding the nature of FCOs. Since the fluxes of only four optical bands are presented in the UDF catalog, we additionally used the UVUDF catalog (Rafelski et al. 2015), which provides fluxes for three UV and four infrared bands, in addition to the optical bands. Furthermore, we independently attained photometry for the Spitzer images; however, the number of detected objects is limited by source confusion due to the large beam size of Spitzer. Figure 11 presents the typical SEDs of four FCOs. The SEDs for the 48 bright FCOs used in analyzing the radial profiles are also shown in figure 21 in appendix 2.

The SEDs in the optical bands are featureless, exhibiting a power-law behavior as expected from the color–color diagram (figure 10). The observed optical SEDs are typically found for starburst galaxies and AGNs. In contrast, excess structures over the power law are found in the infrared bands. Interestingly, the SEDs exhibit a drastic change at the borderline at $1\mu\text{m}$ for almost all bright FCOs.

Rafelski et al. (2015) estimated the photometric redshifts of UDF objects using two evolution models of the galaxy, BPZ and EAZY. The results for UDF objects for which spectroscopic observations have been made and those in figure 11 are shown in table 1, as well as references for previous observations. Small numbers in redshift columns

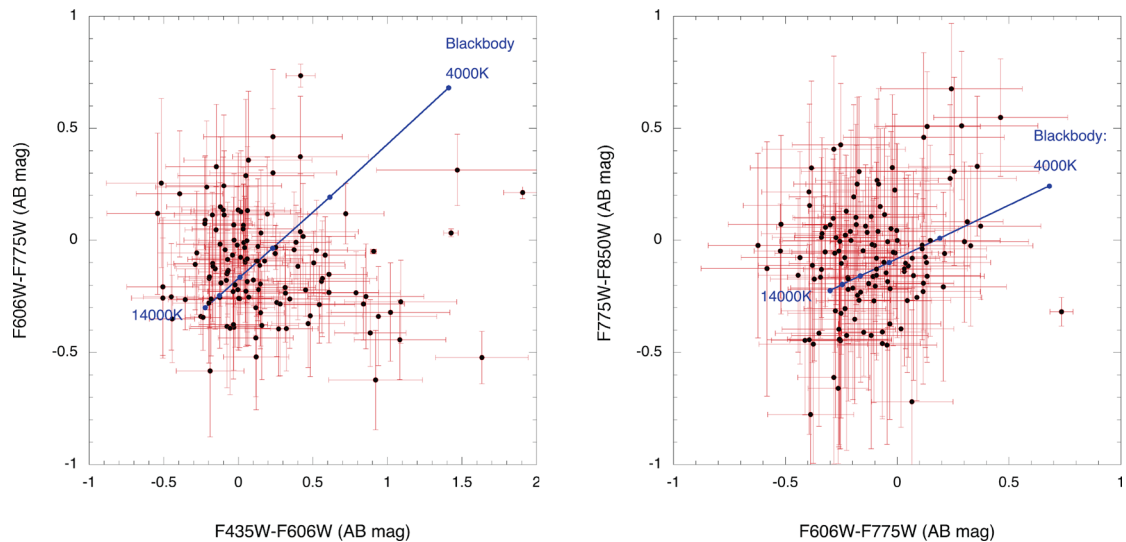


Fig. 10. Color–color diagrams for bright FCOs. The blue solid lines represent the loci of the blackbody. (Color online)

Table 1. Information from bibliographies.*

ID#	UDF #	F775W mag (a)	z BPZ (a)	z EAZY (a)	Emission line detected by MUSE (b)	z MUSE (b)	CONF. [†] (b)	Identification
1	9397	21.031 ± 0.001	1.30–1.42–1.52	0.12–0.17–1.33	H δ , O III	1.2185	2	Quasar (c)
2	7025	25.276 ± 0.006	3.21–3.40–3.59	2.89–2.96–3.04	Ly α	3.326	2	Galaxy (d)
3	6732	24.587 ± 0.006	2.90–3.09–3.27	3.13–3.19–3.25	C III, Ly α	3.1882	2	Quasar (e)
4	4070	25.959 ± 0.01	2.44–2.60–2.75	1.76–1.84–1.91	C III, C III	2.4908	3	Galaxy (d,f)
5	8230	25.531 ± 0.013	3.34–3.54–3.73	3.14–3.22–3.29	Ly α	3.6716	3	Galaxy (d,f)
6	5711	27.353 ± 0.016	0.51–0.59–0.77	0.09–0.12–0.17	H β , H γ , O III, O II, O III, O III	0.6206	3	Galaxy (g,h)
7	8942	27.662 ± 0.033	0.70–0.78–0.85	0.01–0.03–0.05	O III	1.4469	2	Galaxy (g,h)
8	2087	26.597 ± 0.014	3.50–3.72–3.94	3.33–3.42–3.51	Ly α	3.7282	2	Galaxy (d)
12	5550	28.781 ± 0.0533	2.60–2.78–2.95	2.48–2.61–2.80				
14	2047	29.103 ± 0.0708	1.50–1.96–2.35	1.66–2.04–2.42				
16	8858	28.856 ± 0.078	1.54–1.69–1.84	1.59–1.70–1.80				
20	5019	29.155 ± 0.0886	1.27–1.52–2.12	1.37–1.57–1.89				

*References are follows. (a): Rafelski et al. (2015), (b): Inami et al. (2017), (c): Véron-Cetty and Véron (2010), (d): Straatman et al. (2016), (e): Fiore et al. (2012), (f): Cameron et al. (2011), (g): Thompson et al. (2005), (h): Coe et al. (2006).

[†]“CONF.” is a confidence level of the MUSE detection in which “1” corresponds to the best case.

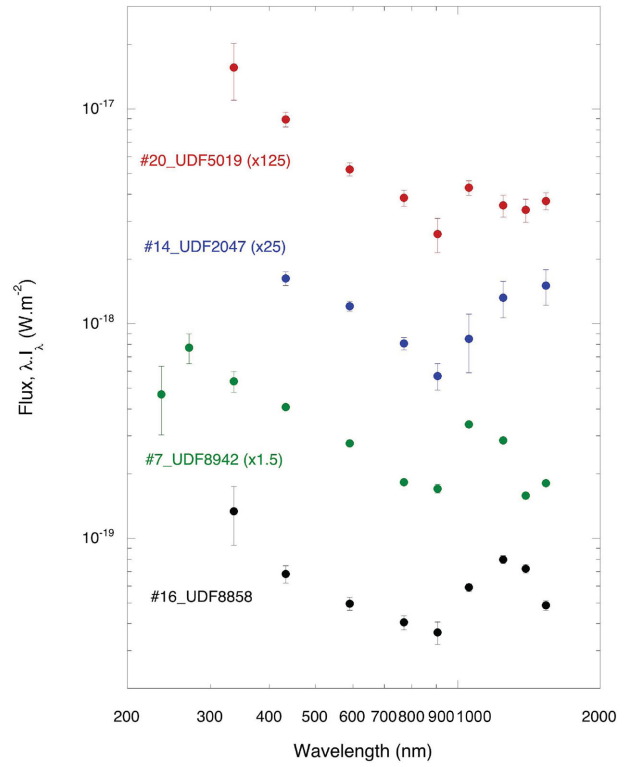


Fig. 11. SEDs of typical FCOs based on the UVUDF catalog (Rafelski et al. 2015). For clarity, the flux scales are magnified as shown in parenthesis. (Color online)

indicate the upper and lower limits of the redshifts with 95% confidence level.

3.2 What are FCOs?

We first examined the known objects similar to FCOs. Globular clusters associated with masked galaxies may be a candidate of FCOs. However, globular clusters have difficulty reproducing the steep slope for the dependence of the surface number density on the magnitude in figure 7, since globular clusters should show a similar slope to the ordinary galaxies. Furthermore, SEDs of FCOs are quite different from those of globular clusters, which consist of late-type stars. This evidence indicates that globular clusters cannot be FCOs.

With respect to compactness, ultra-compact dwarfs (UCDs) are similar to FCOs. However, their SEDs resemble those of late-type galaxies (Drinkwater 2000; Zhang & Bell 2017), which differ from those of FCOs. UCDs are thought to be formed in the the cluster of galaxies by stripping the outer envelopes via collisions with galaxies. UCDs are few in number and localized in cluster of galaxies; thus, they cannot be FCOs.

The third set of candidates is dwarf galaxies undergoing an intense starburst, known as extreme emission line

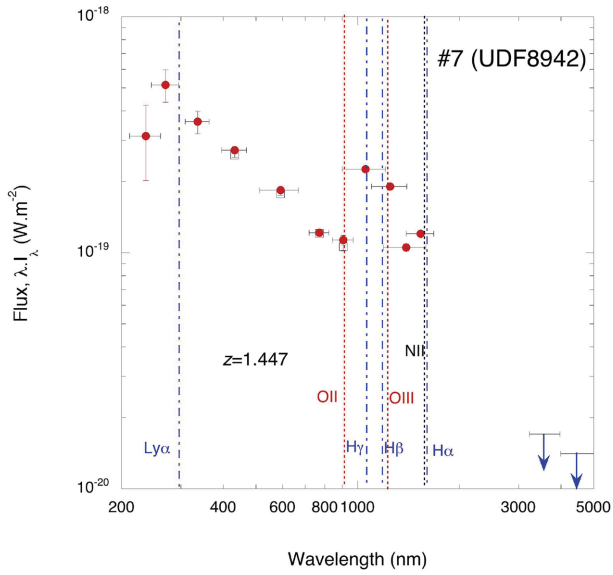


Fig. 12. SED of #7 (UDF8942) compared with the positions of emission lines (filled diamonds and dotted lines), assuming a redshift of 1.447, as reported for MUSE. The red filled circles, open squares, and blue arrows represent the fluxes of the UVUDF and UDF catalogs and the upper limits measured in this work for Spitzer, respectively. The horizontal bars are not error bars; rather, they indicate the bandwidths of the filters. (Color online)

galaxies (EELGs). Such galaxies at a redshift of ~ 2 are characterized by strong [O III] and [N II] line emissions, which show excess infrared emission (van der Wel et al. 2011; Maseda et al. 2013, 2014). FCOs exhibit a similar SED; however, the luminosity of FCOs is much lower than that of EELGs, if FCOs are EELGs.

Inami et al. (2017) attained spectroscopic data for UDF objects using the Multi-Unit Spectroscopic Explorer (MUSE) on Very Large Telescope (VLT) and detected emission lines for eight UDF objects (table 1). The redshifts obtained for seven of these objects which have already been cataloged as quasars or galaxies are reasonably consistent with the photometric redshifts obtained by Rafelski et al. (2015). For the remaining object, #7 (UDF8942), the MUSE result presented [O II] line emission, and the redshift of 1.447 was assigned; however, Rafelski et al. (2015) obtained photometric redshifts of 0.78 (BPZ) and 0.03 (EAZY). The line intensity of [O II] detected by MUSE is $6.74 \pm 1.9 \times 10^{-22} \text{ W m}^{-2}$, which is close to the detection limit, and the redshift was determined from only this line. Figure 12 shows the SED of #7 (UDF8942) and the positions of emission lines expected for a redshift of 1.447. We estimated the line intensity of [O III] by assuming [O III]/[O II] ~ 10 , which is the maximum case for the observed Lyman α emitters and Lyman break galaxies (Nakajima et al. 2016). Even in this case, the contribution of the [O III] line to the $F125W$ band is $5.6 \times 10^{-20} \text{ W m}^{-2}$, which is much lower than the excess flux. No corresponding emission line exists

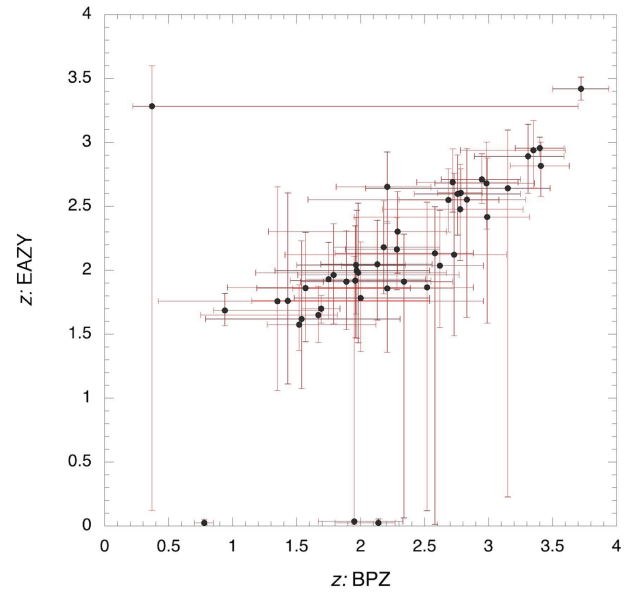


Fig. 13. Correlation diagram for the redshifts obtained from BPZ and EAZY. The error bars represent the allowable range of redshifts listed in the UVUDF catalog (Rafelski et al. 2015). (Color online)

for the excess in the $F106W$ band, and no indication of H α emission is observed for the $F160W$ band. Furthermore, the upper limits of the Spitzer observation exclude the possibility of a Balmer jump for the $1 \mu\text{m}$ excess. Based on these results, we conclude that the redshift of #7 (UDF8942) is not yet determined and that the origin of excess in the $F105W$ and $F125W$ bands is still uncertain. Thus, it is difficult to explain the SED of #7 (UDF8942), as well as SEDs of other bright FCOs (figures 11 and 21), using emission lines.

Since there exists no clear corresponding object for FCOs, we examine the characteristic features of FCOs more carefully. Figure 13 shows the correlation between photometric redshifts obtained from BPZ and those from EAZY (Rafelski et al. 2015), in which two quasars are not included. The errors for EAZY are smaller than those for BPZ; however, the uncertainties are fairly large. The redshift ranges from 1.5 to 3.5 in both cases. In the reported analysis, a lower redshift is defined so that the Lyman α line (121.5 nm) remains in the $F435W$ band, while a larger redshift is obtained by attributing a Balmer jump (364.6 nm) to infrared excess. However, the SEDs in figures 11 and 21 show different features from that expected for the Balmer jump. Thus, we suggest that the photometric redshifts of FCOs obtained by Rafelski et al. (2015) may not be accurate.

Figure 14 presents the magnitude/redshift relation for objects from the UVUDF catalog (Rafelski et al. 2015). The left- and right-hand panels show data for FCOs (stellarity > 0.9) and randomly chosen ordinary galaxies, respectively.

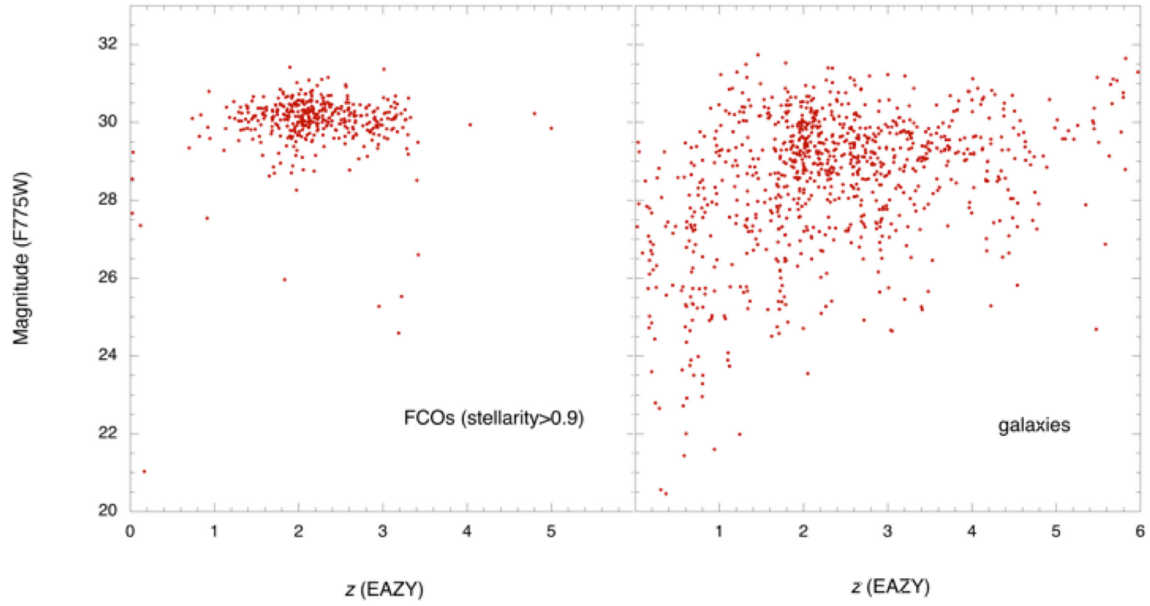


Fig. 14. Redshift (EAZY) dependence on the magnitude at *F775W*. The left-hand panel shows that for FCOs of stellarity larger than 0.9, while the right-hand panel indicates that for the ordinary galaxies randomly chosen from the UVUDF catalog (Rafelski et al. 2015). (Color online)

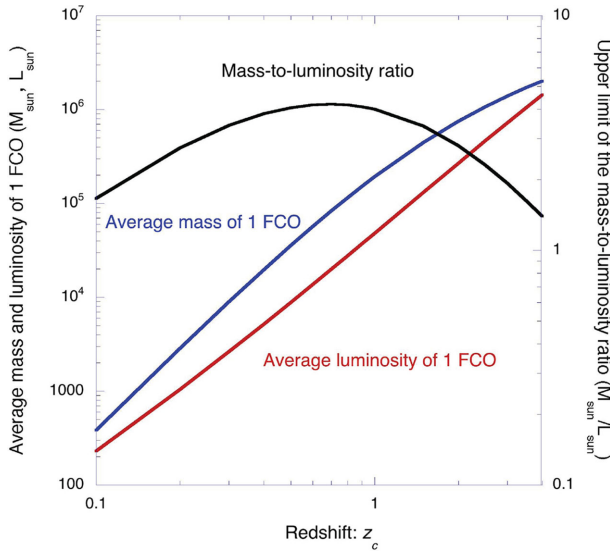


Fig. 15. Dependence of the average luminosity and mass (left-hand ordinate) and mass-to-luminosity ratio (right-hand ordinate) on the redshift, z_c , based on model 1. (Color online)

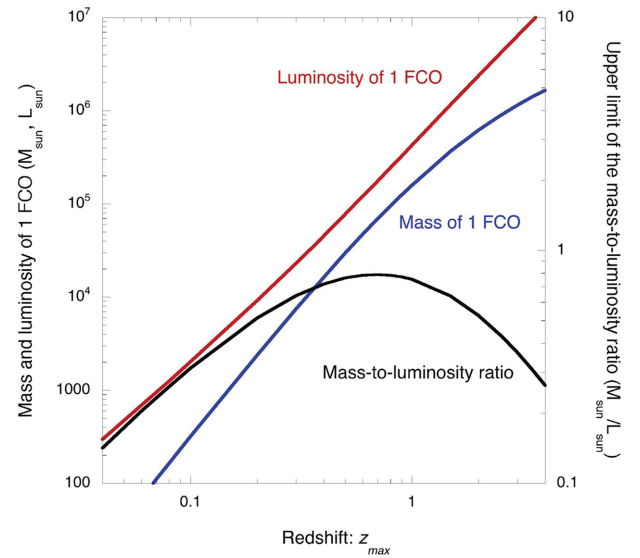


Fig. 16. Dependence of the luminosity and mass of one FCO (left-hand ordinate) and the mass-to-luminosity ratio (right-hand ordinate) on the redshift, z_{\max} , based on model 2. (Color online)

An anomalous feature is observed for the FCOs that is not expected for randomly distributed objects. A simple explanation for figure 14 is that the redshifts of the FCOs (stellarity >0.9) are almost the same; thus, FCOs (stellarity >0.9) are localized at a fixed redshift. This trend is consistent with the SEDs of FCOs (figures 11 and 21), where an SED change at $1\mu\text{m}$ is commonly found. From figure 21, the redshift range of the FCOs is estimated to be $\Delta z/z < 0.1$.

To delineate the nature of FCOs, we used two simplified models. We first assumed that FCOs are located at a fixed

redshift, z_c ($\Delta z/z_c < 0.1$), and have a luminosity function of $\propto 10^{1.2m}$; this is the same shape as the surface number density magnitude relation in figure 7 (model 1). In this model, FCOs appear at certain epochs and disappear after a certain lifetime. The luminosity function can be attributed to the mass difference or elapsed times. We estimated the total flux due to FCOs based on the lower limit of the surface brightness for the *F775W* band, $24\text{ nW m}^{-2}\text{ sr}^{-1}$. Assuming that the optical SED $\lambda I_\lambda \propto \lambda^{-1}$ (figure 10) and that contribution of the sum of the UV and infrared bands

is the same as that for the optical band, we obtained an integrated surface brightness of $47 \text{ nW m}^{-2} \text{ sr}^{-1}$. Since the number of FCOs for the entire sky is 1.38×10^{15} , we can estimate a lower limit of the average FCO luminosity that is dependent on z_c .

Furthermore, we assumed that FCOs consist of missing baryons, corresponding to half of the baryon mass [$2.8 \times 10^9 M_\odot (\text{Mpc})^{-3}$]. We can then obtain the average mass of FCOs and the mass-to-luminosity ratio, depending on z_c . These results are shown in figure 15. The mass and luminosity of FCOs are significantly lower than those of dwarf galaxies, while the mass-to-luminosity ratio of FCOs at $z_c \sim 1$ is a permissible range as dwarf galaxies. However, mass-to-luminosity ratio in figure 15 is over-estimated because the total luminosity is at the lower limit and the existence of faded FCOs is not taken into account.

For the second simplified model, we assumed that the luminosity of FCOs is intrinsically constant (model 2). In this case we attributed the dependence of the surface number density on the apparent magnitude (figure 7) to the radial distribution of FCOs. We applied the spatial density distribution, $n(r) \propto r^3$, where $n(r)$ is the spatial number density of FCOs and r is the comoving radial distance, and assumed that FCOs do not exist beyond r_{max} (z_{max}). This model is the simplest case that satisfies the dependence of the surface number density on the apparent magnitude in figure 7. We attributed the mass of FCOs to missing baryons and applied the same procedure to obtain the integrated luminosity employed in model 1. In this case, FCOs corresponding to the cut-off magnitude, 34.9 mag ($F775W$), are located at z_{max} , which provides the luminosity of FCOs. The number of FCOs was doubled to include faded FCOs, assuming the spatial density of the sum of FCOs and faded FCOs is constant. Figure 16 shows the z_{max} dependence of the luminosity and mass for one FCO, and the mass-to-luminosity ratio. The maximum mass-to-luminosity ratio is 0.79 at $z_{\text{max}} = 0.7$, which is significantly lower than that of ordinary dwarf galaxies; thus, the energy source of FCOs cannot be of a stellar origin.

The two models described above are both overly simplified; thus, actual distribution may fall between the two corresponding predictions. However, the assumption that FCOs consist of missing baryons is confirmed in both models. FCOs contain half of the baryon mass and are major constituents of the universe.

4 Discussion

γ -ray observations are effective for studying the EBL because γ rays are absorbed by collisions with background photons. Biteau and Williams (2015) carefully analyzed all

previous data of the TeV γ observations with redshifts lower than 0.6, and concluded that the obtained EBL is basically consistent with the integrated light of the known galaxies. However, they found an excess EBL at optical wavelengths.

The Fermi-LAT Collaboration (2018) searched for the EBL with lower energy γ -rays, and found that the obtained EBL is consistent with evolution models of galaxies with a redshift range of 0.2 to 3.

These γ -ray observations imply that FCOs must be low-redshift objects, most likely with redshifts lower than 0.1, if FCOs are the source of the excess EBL. Since model 1 is not applicable for such a low redshift, we estimated the properties of FCOs with model 2. For $z_{\text{max}} = 0.1$, the luminosity and mass of FCOs correspond to $1.0 \times 10^3 L_\odot$ and $3.2 \times 10^2 M_\odot$, respectively, and the mass-to-luminosity ratio is $0.32 M_\odot/L_\odot$. The comoving distance for $z_{\text{max}} = 0.1$ is 421 Mpc, and the spatial number density, including faded FCOs, reaches $8.8 \times 10^6 (\text{Mpc})^{-3}$. The distance to bright FCOs (~ 30 mag) for which we measured the radial profiles is 48 Mpc, and the upper limit of the effective radius of $0''.02$ corresponds to 4.7 pc. These results indicate that the energy source of FCOs cannot be of a stellar or nuclear origin and that FCOs are much more compact than an ordinary stellar system with the same mass.

Another important feature is the good correlation between the near-infrared background and the X-ray background. Cappelluti et al. (2013) and Cappelluti et al. (2017) detected a good correlation of the background fluctuation between Spitzer 3.6 and $4.5 \mu\text{m}$, and Chandra soft X-ray bands, [0.5–2] keV. The correlation with harder X-ray bands, [2–7] keV, is marginally significant. The authors showed that the detected correlation at an angular scale of smaller than $20''$ can be attributed to known sources, such as AGNs, starburst galaxies, and hot gas, but residual fluctuation remains at large angular scales. Since the X-ray background has a peak near 30 keV, the X-ray sources responsible for the residual fluctuation may be new unknown objects. Cappelluti et al. (2017) suggested accreting early black holes, including both DCBHs and primordial black holes.

Cappelluti et al. (2017) found that the correlated X-ray background is less than $7 \times 10^{-13} \text{ erg cm}^{-2} \text{ deg}^{-2}$, or $2.3 \times 10^{-3} \text{ nW m}^{-2} \text{ sr}^{-1}$, which corresponds to $\sim 10^{-4}$ of the lower limit of the excess optical background. The ratio is very low compared with an ordinary quasar that has an X-ray emission of $\sim 10\%$ of the optical emission (Elvis et al. 1994). This suggests that the X-ray emission mechanism of FCOs is not so efficient compared to that of the quasars.

Mitchell-Wynne et al. (2016) confirmed the correlation between the Spitzer 3.6 and $4.5 \mu\text{m}$ bands and Chandra soft X-ray bands at small angular scales, but the fluctuation

detected at angular scales larger than $20''$ was not significant. The authors performed an additional correlation study with HST optical and infrared bands ($0.6\text{--}1.6\ \mu\text{m}$), however, they did not obtain a significant correlation because the errors were too large.

Although correlations between the HST optical bands and the Spitzer 3.6 and $4.5\ \mu\text{m}$ bands have not been directly confirmed, we conclude that a certain level of correlation exists between optical and soft X-ray backgrounds, since various combinations of wavelength bands show a good cross-correlation for the wavelength range from the optical to Spitzer bands (Matsumoto et al. 2005, 2011; Zemcov et al. 2014; Mitchell-Wynne et al. 2015).

These features are very similar to those of quasars. FCOs could be powered by gravitational energy associated with a black hole. It may be plausible to regard FCOs as mini-quasars, since the mass and luminosity scales of FCOs are much lower than those of quasars. However, the corresponding emission mechanism, particularly for the infrared excess, is not clear.

FCOs produce not only optical and infrared backgrounds, but also an X-ray background, and are very populous. Even in our vicinity, there exist many faded FCOs, which may originate from gravitational waves (Abbott et al. 2016).

FCOs appear to be major constituents of the universe; however, more observational data are needed to delineate their origin. In particular, spectroscopic observations and deeper surveys with better spatial resolution are needed. Observations toward the different sky regions are also important to examine the effect of the cosmic variance. James Webb Space Telescope (JWST) will play a crucial role in these observations.

5 Summary

We performed a fluctuation analysis for the deepest part of the XDF using four optical bands with the following results.

- Large spatial fluctuations, which cannot be reproduced by ordinary galaxies, are detected for all bands.
- Good cross-correlations between wavelength bands are detected. In particular, an almost perfect cross-correlation is found between the *F775W* and *F850LP* bands.
- The cross-correlation analysis results in a rather flat auto-correlation spectra down to $0''.2$ for the *F775W* and *F850LP* bands. The fluctuation level provides a lower limit of $24\ \text{nW m}^{-2}\ \text{sr}^{-1}$ for the absolute sky brightness, which is significantly brighter than the ILG and is consistent with previous HST and CIBER observations.

As a candidate object responsible for the excess brightness, we identified FCOs that had surface number densities which rapidly increase towards the faint end. FCOs with stellarities larger than 0.9 have the following characteristics.

- The dependence of the surface number density on the *F775W*-band magnitude is found to follow $\propto 10^{1.2m}$.
- The radial profiles of FCOs are indistinguishable from the PSF. Applying de Vaucouleur's law, we found an effective radius r_e of less than $0''.02$.
- The SEDs of FCOs in the optical bands follow a power law, $\lambda I_\lambda \propto \lambda^{-1}$, while the SEDs of the infrared bands show an excess over the optical power law with structure.
- Presuming that FCOs are responsible for the excess background brightness, a cut-off magnitude must reach 34.9 mag for the *F775W* band. In this case, the surface number density of FCOs is $3.35 \times 10^{10}\ \text{degree}^{-2}$.

γ -ray observations require that the excess background brightness have an origin with a redshift below 0.1. This requirement provides restrictions for FCOs, and a simple model renders the following properties for FCOs.

- The luminosity and mass of one FCO are 1.0×10^3 and 3.2×10^2 solar units, respectively.
- FCOs can account for missing baryons.
- The very low mass-to-luminosity ratio implies that the energy source could be powered by gravitational energy associated with a black hole.
- The physical size of FCOs is less than 4.7 pc.

Considering the good correlation between the near-infrared and X-ray background, these results suggest that FCOs may be mini-quasars.

Supplementary data

Supplementary data are available at [PASJ](https://academic.oup.com/pasj/article/71/5/88/5539610) online.

Catalog of detected 1283 Faint Compact Objects.

Acknowledgments

We thank T. Nakagawa, T. Yamada, T. Wada, N. Arimoto, M. Onodera, and M. Ouchi for the constructive discussions and variable comments. We are also grateful to anonymous referee for his/her valuable comments. T. M. would like to thank KASI and ASIAA for providing a good research environment for this work. This work was supported by Japan Society for the Promotion of Science, KAKENHI Grant Numbers 26800112, 17K18789, and 18KK0089.

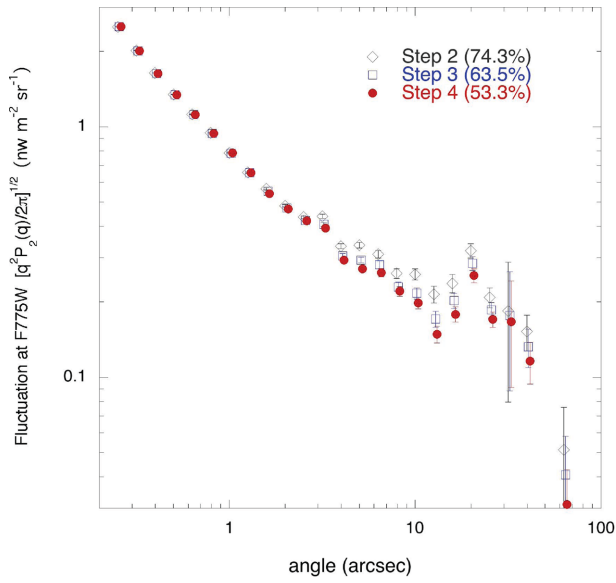


Fig. 17. Dependence of the fluctuation spectra on the depth of the mask level (see text). Horizontal scales are shifted a little to avoid overlap of signals. (Color online)

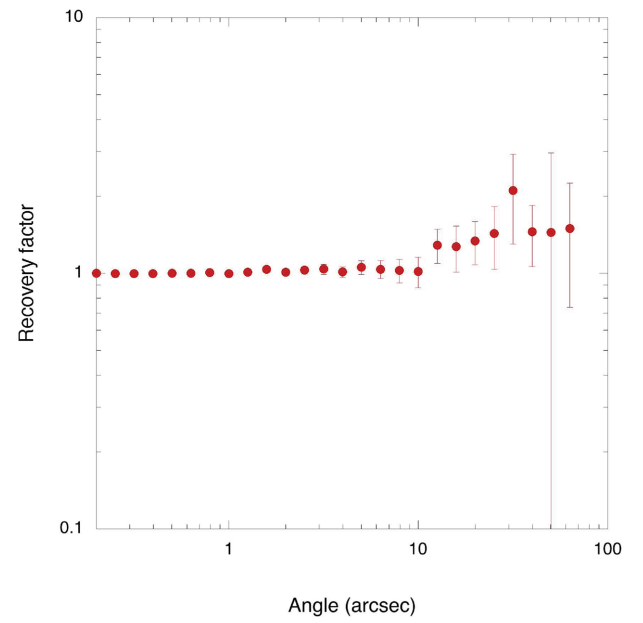


Fig. 19. Recovery factor. (Color online)

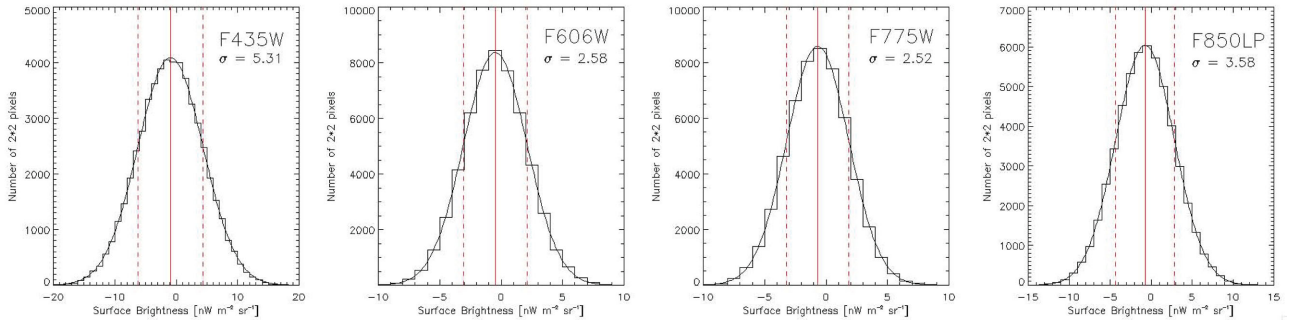


Fig. 18. Histogram on the distribution of the surface brightness for 2×2 pixel resolution. The solid black lines indicate the result of the Gaussian fits. The red vertical solid and dotted lines show the average values and 1σ dispersion levels. (Color online)

Appendix 1 Supplementary information on the masking

We examined the dependence of the fluctuation spectra on the depth of the mask level to confirm the validity of the masking process. Figure 17 shows fluctuation spectra at the *F775W* band after steps 2, 3, and 4 (final). The recovery factors are not adapted to avoid the large errors. Percentages of the remaining pixels are 74.3, 63.5, and 53.3%, respectively. Considering the recovery factor, fluctuation after step 3 is very close to that after step 4,

which indicates that extended wings are well masked after step 4.

Figure 18 shows the histogram on the distribution of the surface brightness for 2×2 pixels resolution. Observed distributions are well fitted by the Gaussian distribution, which is already known in the previous fluctuation analyses (Thompson et al. 2007; Donnerstein 2015).

Figure 19 shows the recovery factor which is obtained by comparing the fluctuations before and after masking. Errors are estimated after 100 simulations.

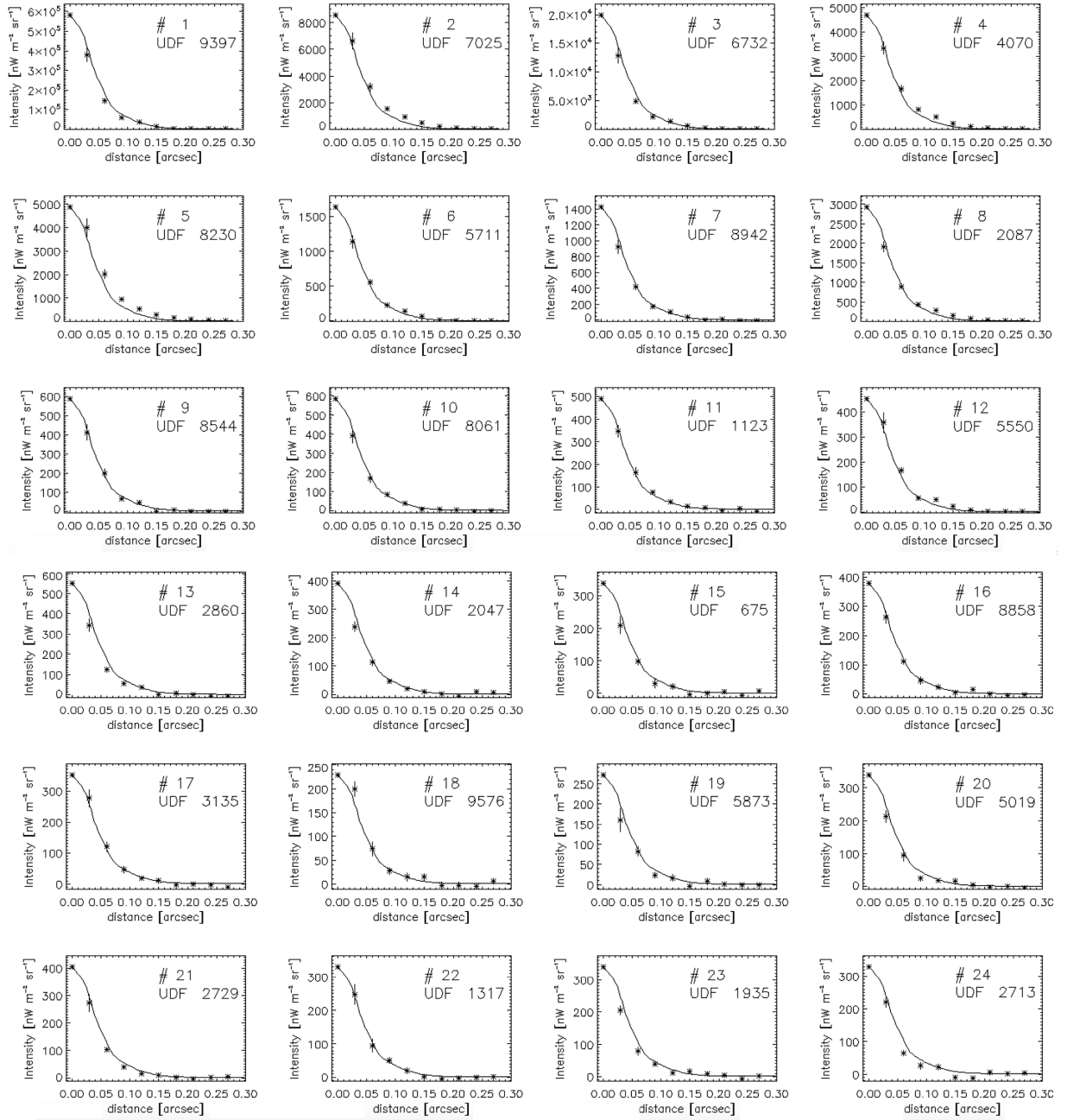


Fig. 20. Radial profiles of bright FCOs for the combined images of *F775W* and *F850LP*. The solid lines present the same radial profiles for the PSF obtained from stars.

Appendix 2 Radial profiles and SEDs for 48 bright FCOs

Figures 20 and 21 present radial profiles and SEDs for bright FCOs, respectively. Radial profiles are obtained for the combined *F606W* and *F775W* images, since the signal-to-noise ratios for the *F435W* and *F850LP* bands are relatively poor. For bright sources, we excluded UDF2710, 6445, and 7307, since the SEDs based on the UDF catalog

are substantially different from those based on the UVUDF catalog. This difference is most likely due to source confusion because their coordinate data are also significantly different. Although the coordinate data for #36 (UDF1240) are consistent, a discrepancy in the SED and a deviation of the radial profile from the PSF are found for this object, which may also be ascribed to source confusion, as there exists another source in the immediate vicinity.

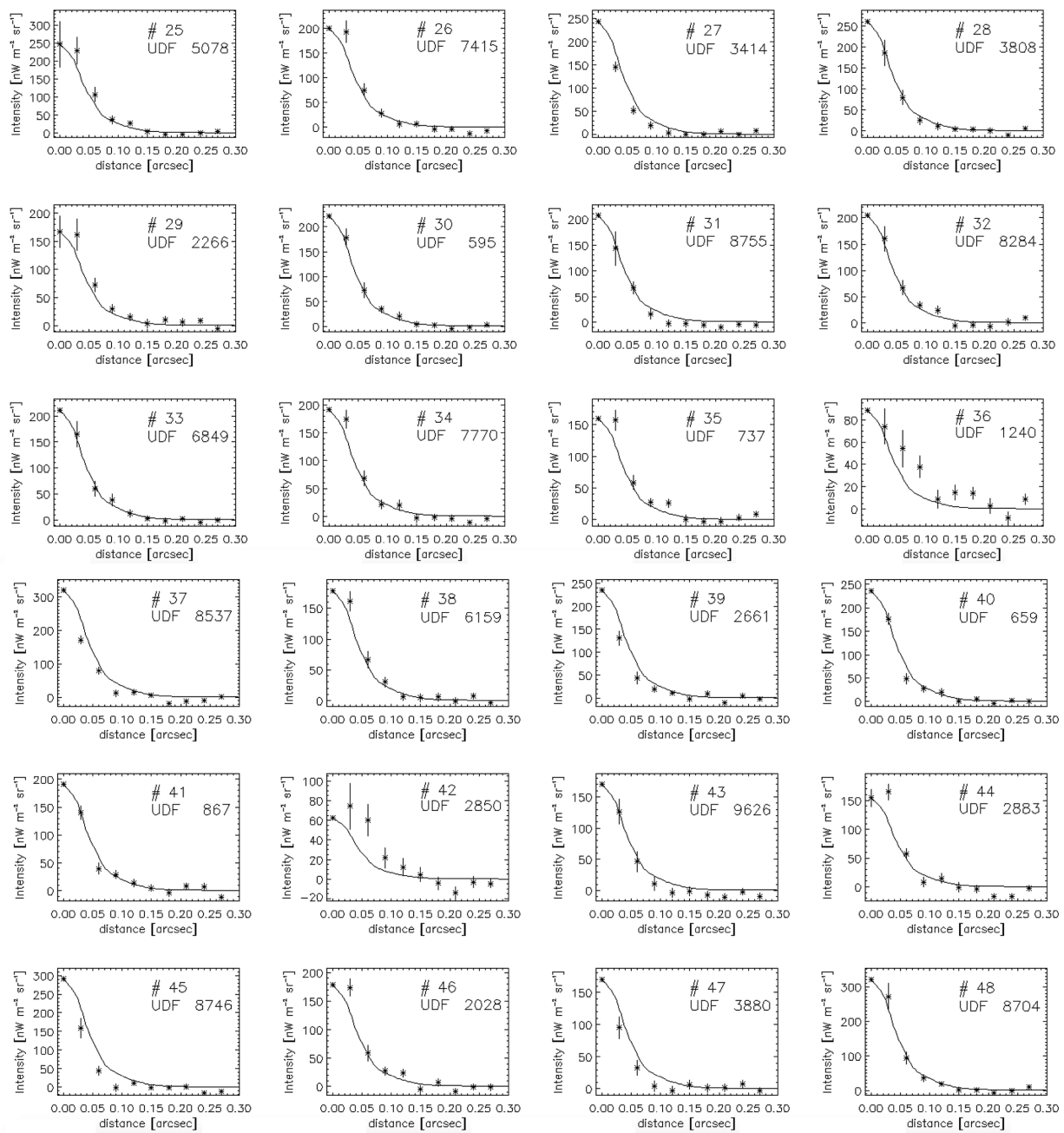


Fig. 20. (Continued)

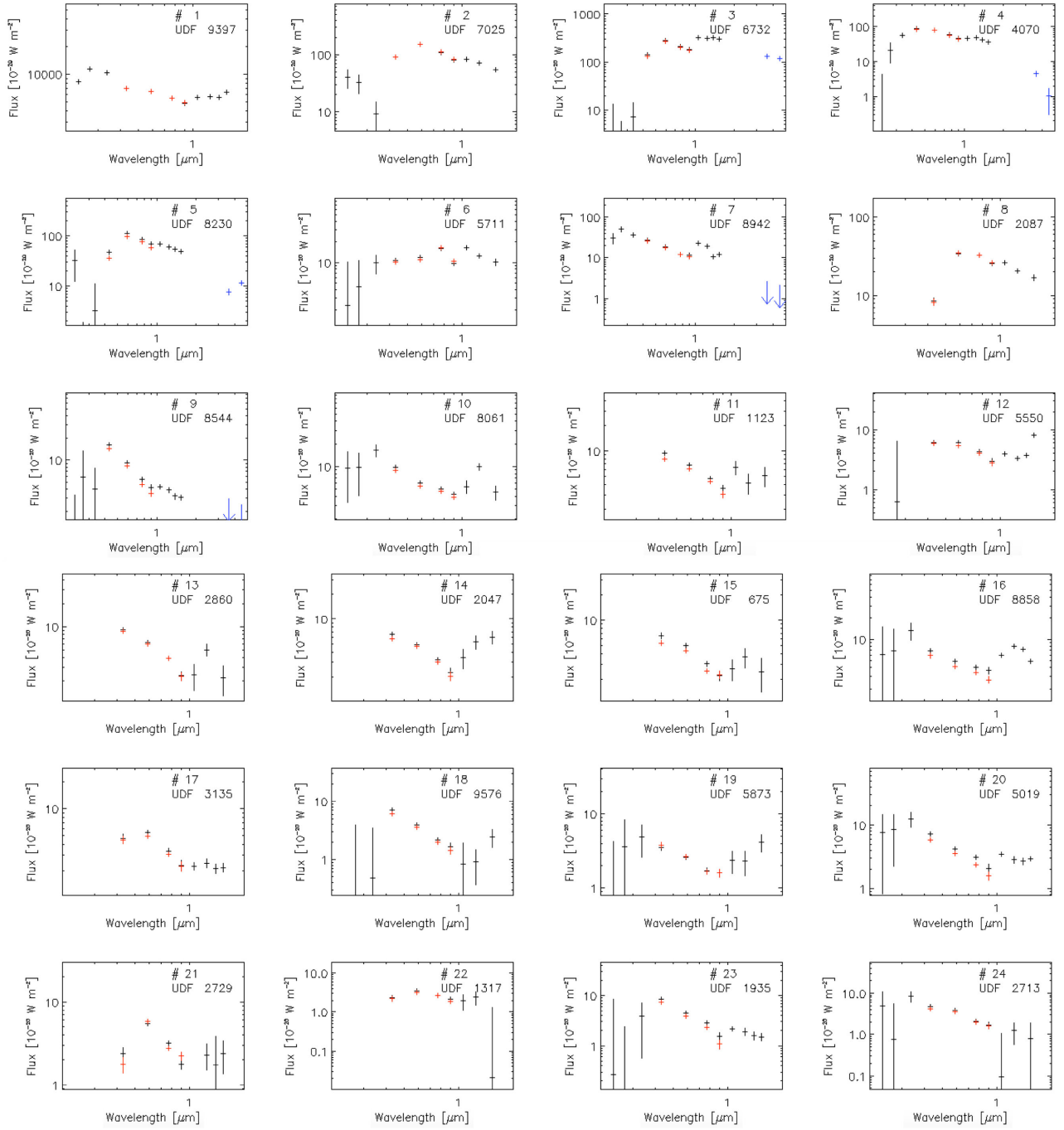


Fig. 21. SEDs of 48 bright FCOs. The vertical bars indicate the errors. The black and red symbols denote the flux values reported by Rafelski et al. (2015) and Beckwith et al. (2006), respectively, while the blue symbols present those of the Spitzer bands as measured in this work. (Color online)

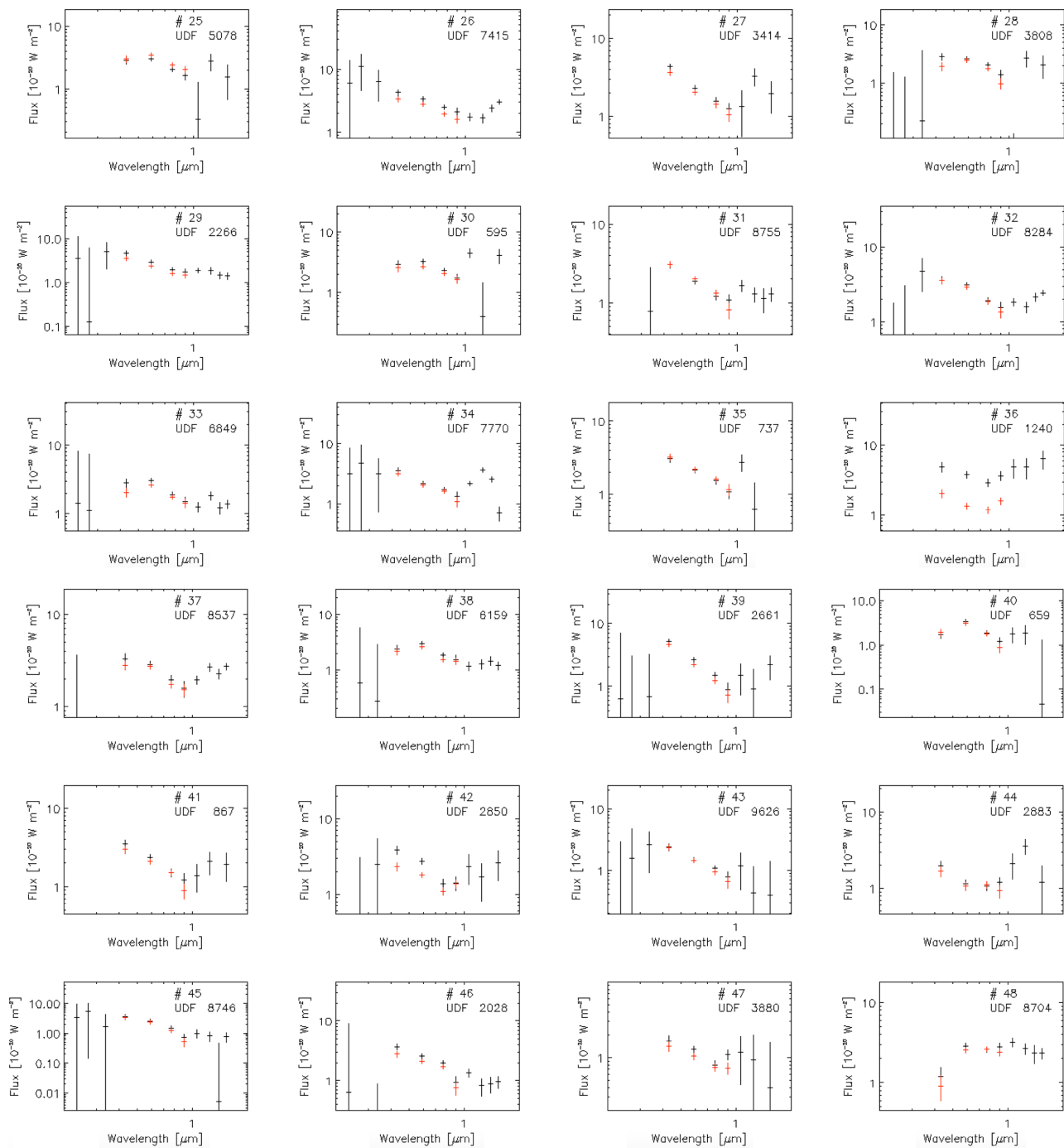


Fig. 21. (Continued)

References

- Abbott, B. P., et al. 2016, *Phys. Rev. Lett.*, 116, 061102
- Beckwith, S. V. W., et al. 2006, *AJ*, 132, 1729
- Bernstein, R. A. 2007, *ApJ*, 666, 663
- Bertin, E., & Arnouts, S. 1996, *A&A*, 117, 393
- Biteau, J., & Williams, D. A. 2015, *ApJ*, 812, 60
- Cambrésy, L., Reach, W. T., Beichman, C. A., & Jarrett, T. H. 2001, *ApJ*, 555, 563
- Cameron, E., Carollo, C. M., Oesch, P. A., Bouwens, R. J., Illingworth, G. D., Trenti, M., Labbé, I., & Magee, D. 2011, *ApJ*, 743, 146
- Cappelluti, N., et al. 2013, *ApJ*, 769, 68
- Cappelluti, N., et al. 2017, *ApJ*, 847, L11
- Coe, D., Benítez, N., Sánchez, S. F., Jee, M., Bouwens, R., & Ford, H. 2006, *AJ*, 132, 926
- Cooray, A., et al. 2012a, *Nature*, 490, 514
- Cooray, A., Gong, Y., Smidt, J., & Santos, N. G. 2012b, *ApJ*, 756, 92
- Donnerstein, R. L. 2015, *MNRAS*, 449, 1291
- Drinkwater, M. J., Jones, J. B., Gregg, M. D., & Phillips, S. 2000, *PASA*, 17, 227
- Elvis, M., et al. 1994, *ApJS*, 95, 1
- Fiore, F., et al. 2012, *A&A*, 537, A16
- Gorjian, V., Wright, E., & Chary, R. R. 2000, *ApJ*, 536, 550
- Hauser, M. G., et al. 1998, *ApJ*, 508, 25
- Helgason, K., Ricotti, M., & Kashlinsky, A. 2012, *ApJ*, 752, 113
- Illingworth, G. D., et al. 2013, *ApJS*, 209, 6
- Inami, H., et al. 2017, *A&A*, 608, A2
- Kashlinsky, A., Arendt, R. G., Ashby, M. L. N., Fazio, G. G., Mather, J., & Moseley, S. H. 2012, *ApJ*, 753, 63
- Kashlinsky, A., Arendt, R. G., Mather, J., & Moseley, S. H. 2005, *Nature*, 438, 45
- Kashlinsky, A., Arendt, R. G., Mather, J., & Moseley, S. H. 2007, *ApJ*, 654, L5
- Kawara, K., Matsuoka, Y., Sano, K., Brandt, T. D., Sameshima, H., Tsumura, K., Oyabu, S., & Ienaka, N. 2017, *PASJ*, 69, 31
- Kim, M. G., Matsumoto, T., Lee, H. M., Jeong, W.-S., Tsumura, K., Seo, H. J., & Tanaka, M. 2019, *PASJ*, 71, 82
- Levenson, L. R., Wright, E. L., & Johnson, B. D. 2007, *ApJ*, 666, 34
- Maseda, M. V., et al. 2013, *ApJ*, 778, L22
- Maseda, M. V., et al. 2014, *ApJ*, 791, 17
- Matsumoto, T., et al. 2005, *ApJ*, 626, 31
- Matsumoto, T., et al. 2011, *ApJ*, 742, 124
- Matsumoto, T., Kim, M. G., Pyo, J., & Tsumura, K. 2015, *ApJ*, 807, 57
- Matsumoto, T., Tsumura, K., Matsuoka, Y., & Pyo, J. 2018, *AJ*, 156, 86
- Matsuoka, Y., Ienaka, N., Kawara, K., & Oyabu, S. 2011, *ApJ*, 736, 119
- Matsuura, S., et al. 2017, *ApJ*, 839, 7
- Mattila, K., Väisänen, P., Lehtinen, K., von Appen-Schnur, G., & Leinert, C. 2017, *MNRAS*, 470, 2152
- Mitchell-Wynne, K., et al. 2015, *Nature Comm.*, 6, 7945
- Mitchell-Wynne, K., Cooray, A., Xue, Y., Luo, B., Brandt, W., & Koekemoer, A. 2016, *ApJ*, 832, 104
- Nakajima, K., Ellis, R. S., Iwata, I., Inoue, A. K., Kusakabe, H., Ouchi, M., & Robertson, B. E. 2016, *ApJ*, 831, L9
- Pirzkal, N., et al. 2005, *ApJ*, 622, 319
- Pyo, J., Matsumoto, T., Jeong, W. S., & Matsuura, S. 2012, *ApJ*, 760, 102
- Rafelski, M., et al. 2015, *AJ*, 150, 31
- Sano, K., Kawara, K., Matsuura, S., Kataza, H., Arai, T., & Matsuoka, Y. 2015, *ApJ*, 811, 77
- Sano, K., Kawara, K., Matsuura, S., Kataza, H., Arai, T., & Matsuoka, Y. 2016, *ApJ*, 818, 72
- Seo, H. J., Lee, H. M., Matsumoto, T., Jeong, W.-S., Lee, M. G., & Pyo, J. 2015, *ApJ*, 807, 140
- Straatman, C. M. S., et al. 2016, *ApJ*, 830, 51
- The Fermi-LAT Collaboration, 2018, *Science*, 362, 1031
- Thompson, R. I., et al. 2005, *AJ*, 130, 1
- Thompson, R. I., Eisenstein, D., Fan, X., Rieke, M., & Kennicutt, R. C. 2007, *ApJ*, 657, 669
- Totani, T., & Yoshii, Y. 2000, *ApJ*, 540, 81
- Tsumura, K., Matsumoto, T., Matsuura, S., Sakon, I., & Wada, T. 2013, *PASJ*, 65, 121
- van der Wel, A., et al. 2011, *ApJ*, 742, 111
- Véron-Cetty, M.-P., & Véron, P. 2010, *A&A*, 518, A10
- Wright, E. L. 1998, *ApJ*, 496, 1
- Wright, E. L., & Reese, E. D. 2000, *ApJ*, 545, 43
- Yue, B., Ferrara, A., Salvaterra, R., & Chen, X. 2013a, *MNRAS*, 431, 383
- Yue, B., Ferrara, A., Salvaterra, R., Xu, Y., & Chen, X. 2013b, *MNRAS*, 433, 1556
- Zemcov, M., et al. 2014, *Science*, 346, 732
- Zemcov, M., Immel, P., Nguyen, C., Cooray, A., Lisse, C. M., & Poppe, A. R. 2017, *Nature Comm.*, 8, 15003
- Zhang, Y., & Bell, E. F. 2017, *ApJ*, 835, L2